Deconvolution method for two-dimensional spatial-response mapping of lithographic infrared antennas

Javier Alda, Christophe Fumeaux, Iulian Codreanu, Jason A. Schaefer, and Glenn D. Boreman

The spatial impulse response of antenna-coupled infrared detectors with dimensions comparable with the wavelength is obtained from a two-dimensional scan of a tightly focused CO_2-laser beam. The method uses an experimental setup with submicrometer resolution and an iterative deconvolution algorithm. The measured spatial response is compared with numerically computed near-field distributions of a dipole antenna, with good agreement. © 1999 Optical Society of America

OCIS codes: 040.0040, 040.3060, 040.5570, 100.1830, 230.5440.

1. Introduction

Novel submicrometer-sized thin-film detectors have been demonstrated in the infrared (IR) at wavelengths near 10 μm. Their sensing mechanism is based on the operation of metal–oxide–metal (MOM) diodes[1–3] or microbolometers.[4] The power collection capability of these ultrasmall detectors is enhanced by the use of integrated antennas. The measured response is closely related to the shape of the antenna (e.g., dipole, bow tie, or spiral) and its physical dimensions. These detectors are the smallest currently available in the IR region. Characterization of their two-dimensional spatial response is therefore a challenging task. In this paper, we demonstrate a method to map the spatial response of these devices.

The signal obtained from a detector is proportional to the irradiance distribution integrated over the collecting area of the device. For classical macroscopic IR sensors the photosensitive region is well defined and is usually described as an effective area within which a constant spatial response is assumed; the outside region is zero. To characterize such devices, one typically scans a probe beam across the photosensitive region, measuring the output of the detector as a function of the position of the probe beam. The measured output signal is, in general, the convolution of the sensor's spatial response and the beam profile. If the dimensions of the photosensitive region are large compared with the beam, the detector's spatial response can be approximated directly as the measured output signal.

The subwavelength IR detectors used in our study are smaller than the waist dimensions of laser beams, even when low $f/\#$ focusing optics are used. Consequently, our problem involves the mapping of a structure smaller than the dimension of the probe beam used for the measurement. This problem has been addressed and solved in other areas of optics. The restoration of images produced by aberrated systems is possible when the transfer function of the optical system is well known. An interesting application of this principle was developed for the Hubble Space Telescope.[5] Its point-spread function (PSF) was calculated with high accuracy, and blurred images were enhanced by use of the known PSF in a deconvolution procedure. The algorithms developed for this case have been adapted to retrieve the spatial response of our small IR detectors.

Section 2 describes the theoretical foundations of the deconvolution method and shows the application of the iterative algorithm, along with the characterization method of the illuminating beam and the parameterization of the spatial response. To illustrate the deconvolution method, we present in Section 3 the determination of the thermal and the antenna spatial response of MOM antenna-coupled detectors. The practical problems of characterizing the beam before the deconvolution algorithm are discussed. We also analyze several methods to provide dimen-

sional parameters that describe the collecting area of the detectors. The results of the method are compared with the near-field distribution of a dipole antenna.

2. Measurement of the Spatial Response

When an arbitrary irradiance distribution falls onto a detector, the signal is obtained by integration of the spatial distribution of the irradiance over the receiving area of the detector. This fact can be expressed as

$$S = \int\int_{-\infty}^{\infty} I(\mathbf{r})D(\mathbf{r})\mathrm{d}r, \qquad (1)$$

where $I(\mathbf{r})$ is the incident irradiance distribution and $D(\mathbf{r})$ is the spatial response of the detector, with $\mathbf{r}$ being the vector position on the plane of the detector.

Our method to determine the spatial response of the detector is based on a two-dimensional scan of the receiving area with a probe beam. The detector signal, $S(x, y)$, is recorded as a function of the sensor's position with respect to the beam. It is given by the convolution:

$$S(x, y) = I(x, y)*D(x, y)$$
$$= \int\int_{-\infty}^{\infty} I(x', y')D(x - x', y - y')\mathrm{d}x'\mathrm{d}y'. \quad (2)$$

The detector's spatial response function, $D(x, y)$, can be obtained if both $I(x, y)$ and $S(x, y)$ are known.

The detectors that we want to characterize are smaller than the beam. The beam has a typical minimum waist area of approximately $\pi(1.22\lambda)^2$, whereas the effective collecting area of the detector is known to be only a fraction of λ^2, as stated by Fumeaux et al.[6] The success of our deconvolution method depends on an accurate knowledge of the beam and on achievement of a high signal-to-noise ratio in the detector response.

A. Beam Measurement and Characterization

To produce an accurate deconvolution, we need a good characterization of the probe beam at the plane of the measurement (in the case of image restoration this corresponds to a faithful characterization of the PSF). The plane is chosen to be that of the beam waist where the irradiance reaches its maximum value. Although, ideally, one considers a diffraction-limited beam, the uncertainties in alignment may introduce some residual aberration. Therefore we expect a beam with a characteristic waist area of approximately $10\ \lambda^2$. Pixelated IR imaging systems do not have sufficient spatial resolution to provide a fine enough sampling of such a tightly focused laser beam. Consequently, we used a scanning method to characterize the beam.[7] A knife edge is moved across the beam along two orthogonal axes for several axial positions.[8,9] The light that is not blocked by the knife edge is detected by a large-area thermal IR detector. The data are an integral of the beam and are used to

develop a model of the beam profile. If the intensity distribution of the beam is $I(x, y, z)$, the knife-edge signals are given by

$$K(x, z) = \int_{-\infty}^{x}\int_{-\infty}^{\infty} I(x', y, z)\mathrm{d}x'\mathrm{d}y, \qquad (3)$$

$$K(y, z) = \int_{-\infty}^{\infty}\int_{-\infty}^{y} I(x, y', z)\mathrm{d}x\mathrm{d}y'. \qquad (4)$$

We found the position of the beam waist by analyzing the Z-axis evolution of the measured functions $K(x, z)$ and $K(y, z)$. These functions reach a maximum steepness at the beam-waist plane, $z = z_\omega$. Although in the one-dimensional case it is possible to retrieve the beam profile from a single knife-edge measurement, this is not the case for a general nonsymmetric beam. Thus a two-dimensional model of the beam is developed from the knife-edge data sets, $K(x, z_\omega)$ and $K(y, z_\omega)$, and a simulated knife-edge response is calculated. The beam parameters are optimized to yield a best fit of the experimental data. The selection of the function representing the best fit to the probe beam depends on the particular characteristics of the laser source, the focusing setup, and the information extracted from the measured data, e.g., the orientation and relative amount of coma and the presence of diffraction rings. A Gaussian beam is a reasonable starting point for a beam profile, if the focusing optics are sized to avoid hard-aperture effects. The beam model is then refined by the addition of aberrations and diffractive terms as necessary.[10–12]

B. Deconvolution Method

When the spherical-aberration problem of the Hubble Space Telescope was discovered, a considerable effort was made to develop a method for enhancing the quality of the images. The PSF of the system was modeled and used for deconvolving the images. Some of the algorithms used in that case can be applied to our problem. A particularly succesful method is the Richardson–Lucy algorithm,[13–15] an iterative process that converges to the maximum-likelihood solution of the function before blurring. For our case it can be written as follows:

$$D^{k+1}(x, y) = D^k(x, y)$$
$$\times \frac{\int_{-\infty}^{\infty}\int_{-\infty}^{\infty} \dfrac{S(x', y')}{S^k(x', y')} I(x - x', y - y')\mathrm{d}x'\mathrm{d}y'}{\int_{-\infty}^{\infty}\int_{-\infty}^{\infty} I(x', y')\mathrm{d}x'\mathrm{d}y'}, \quad (5)$$

where S represents the measured data, I is the input irradiance distribution, and D^k is the spatial response of the detector obtained at the kth step of the
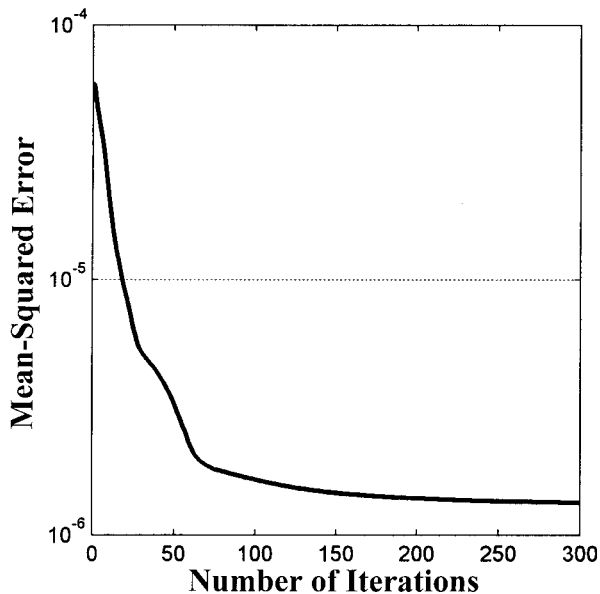
Fig. 1. Evolution of the MSE between the actual measured data and the image obtained for every step. The MSE decreases sharply during the first steps of the algorithm and then becomes stable.

Fig. 2. Schematic experimental setup used for measuring the spatial response of the detectors.

algorithm. A calculated version of the signal S^k is obtained with the convolution:

$$S^k(x, y) = D^k(x, y) * I(x, y). \tag{6}$$

We describe the accuracy of the deconvolution by means of the mean-squared error (MSE) between our experimental data and $S^k(x, y)$. As seen in Fig. 1, the MSE stabilizes after a fast decrease during the first steps of the algorithm. If the algorithm is left running without limitation in the number of steps, it will try to reproduce the noise of the measured image by a fragmentation of the object. This fact can be monitored because the MSE shows a sharp increase when a fragmentation appears. Then, we chose to stop the algorithm after initial stablization of the MSE. The typical number of iterations used is near 300.

An important difference between our measurements and the typical image enhancement case is that our image is obtained after a long scanning procedure that takes approximately 90 min. Therefore it is not practical to average several images to obtain a lower noise level. This noise places a lower limit on the MSE achievable.

C. Characteristic Parameters of the Spatial Response

Although the two-dimensional spatial response gives insight into the detailed behavior of the antenna, it is more convenient in practice to provide a simpler characterization in terms of the size of the receiving area. This area can be used as a figure of merit for comparison with other devices.

A first approach to model this area is to assume an elliptical shape,[6] then the characterization is given by the axes of the ellipse and its orientation. The ratio
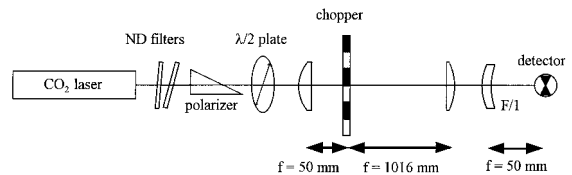
of the axes describes the aspect ratio of the spatial response. This allows us to determine the element-to-element spacing along two orthogonal directions in an IR focal-plane array. The ellipse characterization can be done with the same procedures applied to laser beams,[16] in terms of the moments of the spatial response function.

It is also possible to define the receiving area as a flat-top function for which the shape of the base is given by a ratio between the enclosed volume within the area and the total volume under the spatial response. The area can be computed with the contour that encircles the main part of the volume (for example, 90%). Use of this area facilitates a convenient estimation of the power collected by the detector for a certain level of irradiance. This collected power is relevant for description of detector performance, either in terms of responsivity or noise-equivalent power. This collection area also indicates the maximum allowable spacing of detector elements that can be used to achieve an efficient power collection.

From a spatial-resolution viewpoint, an optimum arrangement of detectors can be achieved if the spatial responses of two adjacent detectors intersect at the 50% point. Therefore the area that encircles the half of the volume of the spatial response indicates the maximum density of detectors for an optimization of the resolution of a focal-plane array.

3. Spatial Characterization of Metal–Oxide–Metal Infrared Antennas

The devices that we characterized with this method are MOM junctions coupled to a dipole antenna whose full length is approximately 6.7 µm.[1,2] They show a marked polarization dependence, a fast response, and other features that make them a promising device for IR imaging.[6] To obtain a thorough characterization of the device, it is necessary to measure the spatial response for two polarizations, one with the electric field parallel to the antenna axis and the other with the electric field perpendicular. The current waves induced in the arms make the parallel response larger than the perpendicular one. The parallel response can be modeled as the sum of two contributions: one arising from a polarization-independent thermal effect in the substrate and the other arising from the antenna response.[2,3] We characterized three antenna-coupled MOM sensors that were fabricated on the same chip and that showed a similar responsivity and polarization dependence.
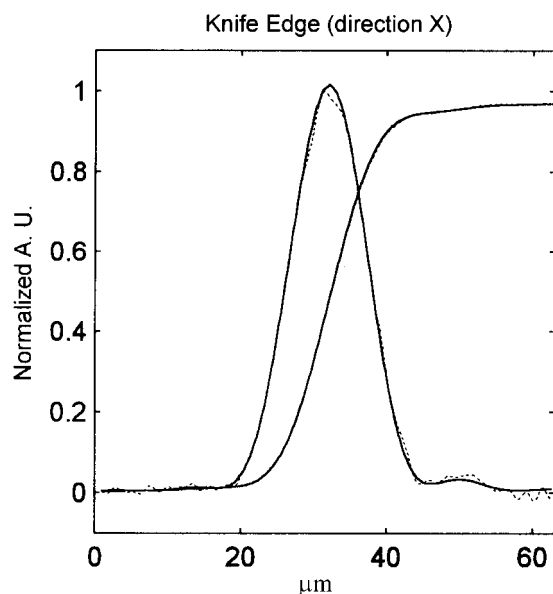
Knife Edge (direction X)

Fig. 3. Comparison of the simulated knife edge obtained with the modeled beam (solid curve) and the experimental data for the beam-waist position (dotted curve). The knife edge is along the x direction.

A. Experimental Setup

The experimental setup is presented in Fig. 2. The beam is delivered by a CO_2 laser emitting in the $10P(20)$ line at $\lambda = 10.59$ μm with a TEM_{00} mode. A set of neutral-density filters is used to attenuate the beam and to reduce the optical power in the focused spot to 25 mW. The polarization of the beam is fixed by means of a pile of plates oriented at the Brewster's angle. To rotate the plane of polarization, we used a half-wave plate after the polarizer. The laser beam was focused onto the device by means of a set of three lenses. The first lens focused the beam onto a plane where a mechanical chopper was placed. A second lens collimated this radiation and filled the aperture of the third lens, an aspheric designed to be free of spherical aberration for an object at infinity. This aspheric operates at $f/1$. The antenna is illuminated through the substrate to avoid interference effects[6] and to produce a better coupling of the radiation to the antenna–detector structure.[17]

The device was mounted on a three-axis micropositioner stage. The movement along the beam-propagation direction, Z, was controlled manually. The X and the Y motions were motorized with a Melles–Griot Nanomover system and were controlled by a computer that also controlled the data aquisition. The sensor was connected to a current biasing source and a preamplifier whose signal was directed to a lock-in amplifier synchronized with the mechanical chopper. The beam waist was located by movement of the detector along the three axes and by a maximizing of the response. Once the device was located at the beam waist, the Z position (along the axis of propagation of the beam) was fixed, and a two-dimensional serial scan was performed, moving
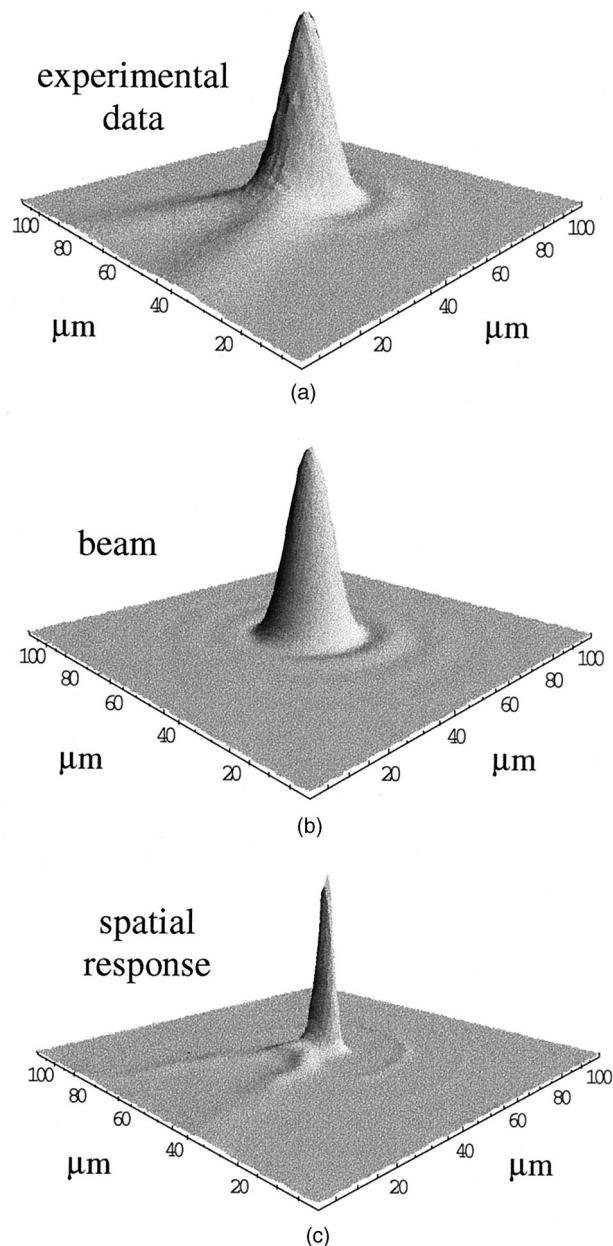

Fig. 4. (a) Measured image obtained from the experimental setup. (b) Beam used for deconvolving the data. (c) Spatial response obtained after 300 iterations of the deconvolution algorithm.

the device in the X and Y directions. Our measurements were made along a square of 100 μm, with steps of 1 μm and a repeatability of 0.1 μm. The 10,000 data points were acquired in 1.5 h with our experimental setup. Each detector was scanned four times. The response for the perpendicular and the parallel polarizations were measured for two orthogonal orientations of the detector with respect to the beam. Rotating the devices 90° in the XY plane for each polarization yielded additional insight on the beam structure and provided additional data for the deconvolution procedures. For each polarization, a total of six spatial responses were obtained from the

(a)

(b)

(c)
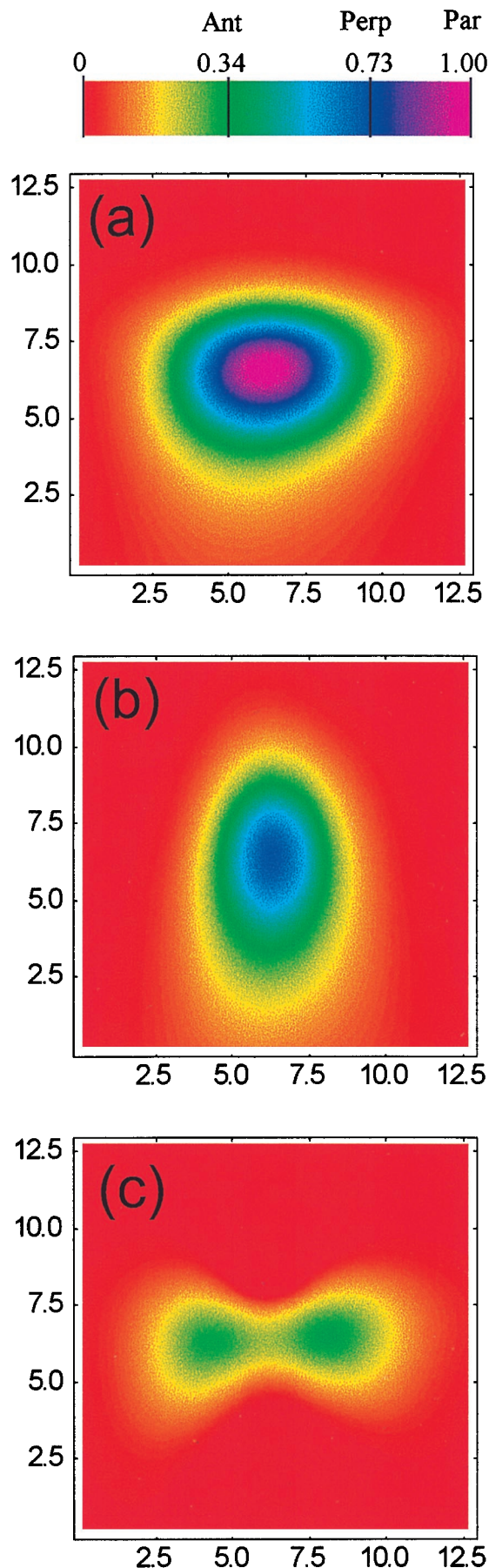
three devices. To increase the signal-to-noise ratio of the measurement and to decrease uncertainties accumulated along the calculation process, we averaged these responses after adjusting their mutual orientations.

B. Beam Characterization

When the laser beam is focused by the aspheric lens, the incoming collimated beam is larger than the diameter of the lens, producing a focusing spot having a primarily Airy-function character. In addition, residual alignment errors in the setup produced a small amount of coma, less than $\lambda/20$, in the focused beam. The comatic aberration was seen in a well-defined angular direction. Thus the beam is modeled as a convolution of the Gaussian beam delivered by the laser and the comatic Airy function.[10] The analytical expression of this model is given by the formula:

$$
E(x, y) = \exp\left(-\frac{x^2 + y^2}{\omega_0^2}\right) * \left(\frac{2J_1(v)}{v} - \alpha \cos\phi \frac{2J_4(v)}{v}\right.
$$

$$
-\alpha^2 \frac{1}{2v} \times \left\{\frac{J_1(v)}{4} - \frac{J_3(v)}{20} + \frac{J_5(v)}{4} - \frac{9J_7(v)}{20}\right.
$$

$$
\left.\left.- \cos 2\phi\left[\frac{2J_3(v)}{5} + \frac{3J_7(v)}{5}\right]\right\}\right), \qquad (7)
$$

where J_k are the J-Bessel functions of order k, ϕ is the orientation of the comatic spot, α is the amount of coma in wavelength units, and

$$
v = \frac{2\pi}{\lambda} \frac{a}{z} (x^2 + y^2)^{1/2}, \qquad (8)
$$

where a is the radius of the circular aperture and z is the distance from the aperture to the plane of focus.

The knife-edge measurements[9] were compared with the results of the analytical model. An optimization procedure was then performed to find the beam parameters. In Fig. 3 we show how the results of a simulated knife-edge scan (solid curve) of the modeled beam compared with the experimental results (dotted curve). The best fit the experimental knife-edge data produced an input beam with the following parameters: $\omega_0 = 5.5$ μm, $\alpha = 0.033$, $\phi = 325°$, $a = 23.1$ mm, and $z = 50$ mm. These parameters are consistent with their expected values, when the laser characteristics, the actual dimensions of the lenses and their focal lengths, and the alignment precision are considered. The modeled beam that we used in the deconvolution is represented in Fig. 4(b).

Fig. 5. Average spatial response obtained after deconvolution of the experimental data. The direction of the electric field is (a) parallel and (b) perpendicular to the dipole antenna. The antenna response is obtained by substraction of both responses and is represented in (c). The scale on the top shows the relative value of the maximum for each of the spatial responses: parallel (Par = 1.00), perpendicular (Perp = 0.73), and the antenna (Ant = 0.34). The spatial dimensions are given in micrometers.

C. Deconvolution

The Richardson–Lucy algorithm was applied to the experimental data with the modeled beam obtained from the knife-edge measurements. The thermal response was assumed to be represented by the deconvolution of the image obtained for the perpendicular direction of polarization.[6] The spatial responses for both polarizations were subtracted to obtain the antenna's spatial response.

Figure 4 shows the measured data, the beam used in the deconvolution, and the sensor's spatial response obtained after 300 iterations. When the sensor's response and the beam are convolved again, the results are visually undistinguishable from the measured signal. Although we are mainly interested in the measurement of the antenna and the thermal responses, it is possible to observe the response of the coplanar strips that make the low-frequency connection to the bond pads. Approximately the same magnitude (~3% of the maximum of the parallel spatial response) is seen for both the parallel and the perpendicular polarizations, showing the mainly thermal character of the bond-pad response.

D. Thermal and Antenna Responses and Their Spatial Characterization

In Fig. 5 we present the average of the spatial responses of the devices. There are several reasons why an averaging procedure is desirable. First, the modeled beam was obtained by our fitting an integral representation instead of a point-to-point map of the beam. The location and size of the beam waist were found by our averaging and fitting the knife-edge measurements. Second, the experimental data contains a level of noise that limits the number of iterations allowed in the algorithm. After analyzing the histogram of the scans, we evaluated the level of noise to be approximately 2% of the maximum value for the perpendicular polarization case, which corresponds to an approximate value of 1% the copolarized signal. Finally, there are the experimental uncertainties due to the positioning of the device along the Z axis and the residual long-term variation of power of the laser source.

The spatial response to the parallel polarization [Fig. 5(a)] can be distinguished from the perpendicular one [Fig. 5(b)], not only because of its higher amplitude (see scale at the top of Fig. 5 showing the maximum of the perpendicular and the antenna responses normalized to the maximum of the parallel) but also because of its shape that is aligned along the direction of the dipole. Once the deconvolution has been made for each set of data, the antenna response is obtained by substraction of the spatial responses of the parallel- and the perpendicular-polarization directions. The average of these results is shown in Fig. 5(c).

From a practical point of view it is more convenient to characterize the receiving area by a few parameters instead of by a map of its variation. These parameters have been discussed in Subsection 2.C.
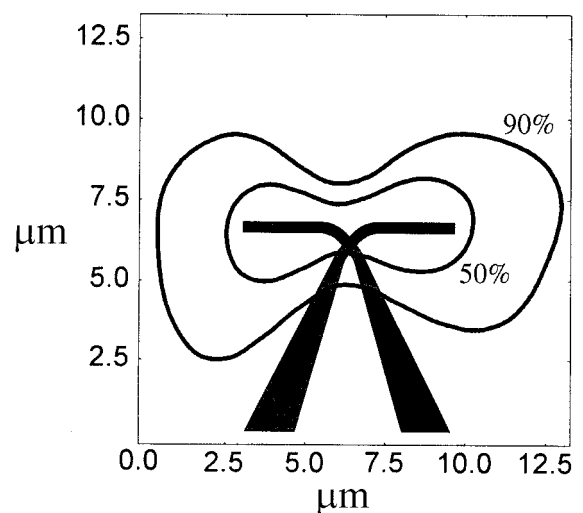
Table 1. Characteristic Parameters of the Spatial Response of the Antenna[a]

Characteristic Parameters of the Antenna Response	
Parallel semiaxis of the ellipse (μm)	6.2 ± 0.5
Perpendicular semiaxis of the ellipse (μm)	3.1 ± 1.0
Area encircling 90% volume (μm^2)	58.6 ± 18.9
Area encircling 50% volume (μm^2)	17.7 ± 3.8

[a]The values are the average of the parameters obtained from the individual spatial responses of the six measurements plus/minus their standard deviation.

The computed area parameters for the antenna response are presented in Table 1. The values are the average and the standard deviation of the parameters obtained for the six individual spatial responses. The contours of the areas that encircle 50% and 90% of the volume of the antenna spatial response are represented in Fig. 6, superimposed with the geometry of the antenna-coupled detector. The correlation between the geometry of the antenna and its deconvolved spatial response is significant. In Subsection 3.E this correlation is corroborated by the results from two numerical simulations of the dipole antenna.

Previously, the spatial response was modeled as a rectangular function having an elliptical base.[6] The measurements made along the two principal directions allowed the dimensions of the ellipse to be determined. Here the values of the semiaxes of the ellipse are obtained from the deconvolution by means of the calculation of the moments of the spatial response. The results are in good agreement with the conclusions of Fumeaux *et al.*[6] who estimated that the effective area of the antenna response extended approximately one dielectric wavelength ($\lambda_{Si} \simeq 3.1$ μm) past the physical dimensions of the antenna on each side in the two principal directions. For our

Fig. 6. Geometric structure of the antenna-coupled detector is represented along with the contours of the areas containing 50% and 90% of the volume of the spatial response. The lobes corresponding to the arms of the antenna are clearly distinguished.
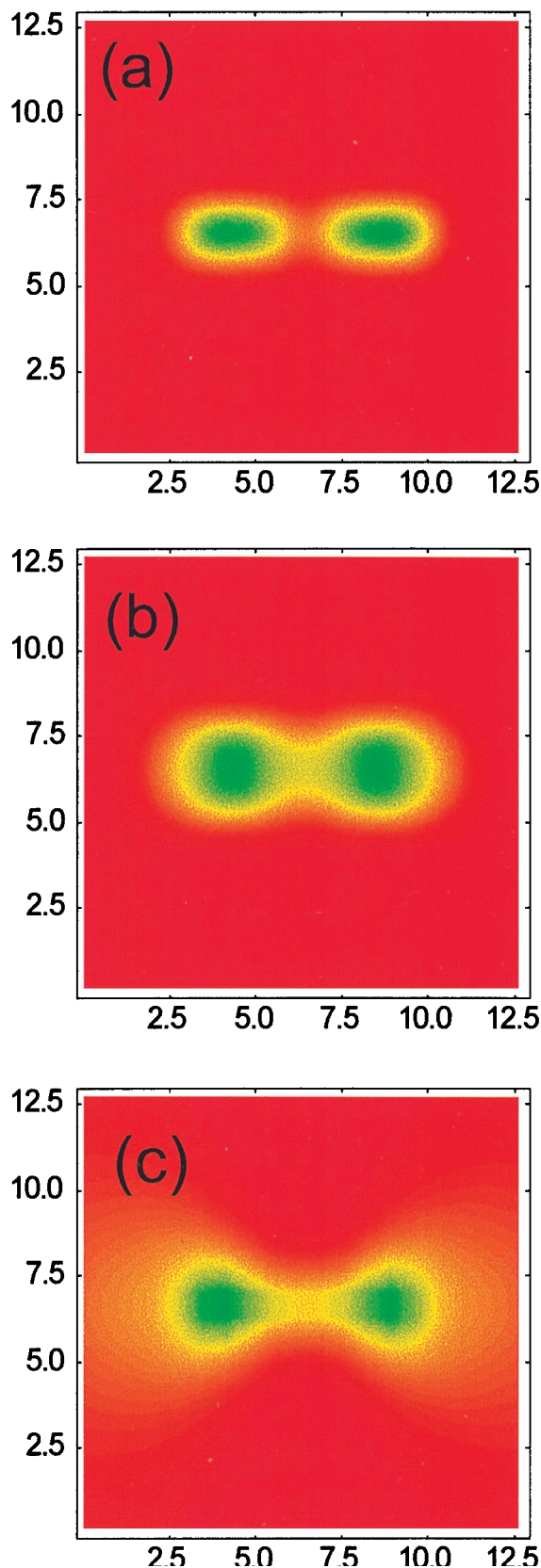
(a)

(b)

(c)

6.7-μm-length antenna this estimation would result in a horizontal and a vertical semiaxis of 6.4 and 3.1 μm, respectively. These values can be successfully compared with those referred to in Table 1.

In addition to this ellipse characterization, the other parameters of Table 1 can be used according to the desired application. For example, the area encircling 90% of the volume can be used for the estimation of the collected power in the calculation of the responsivity of the detector. Despite the tight focusing, only 3.3 of the total 25-mW beam power was enclosed by this collecting area. This yields a responsivity of approximately 0.1 V/W for the detectors used in this study.

E. Simulation of the Antenna Near-Field Distribution

The results discussed the last section were compared with two simulations of the antenna response. The calculation was performed with a full-wave, method-of-moments[18] electromagnetic simulation package (IE3D from Zeland Software Inc.).

In the first simulation, we evaluated a simple model of a dipole immersed in vacuum with the wavelength taken to be the effective wavelength in the Si substrate, $\lambda_{Si} = 3.1$ μm. To scale the real dipole, a 2.2-λ_{Si}-long, 1/15-λ_{Si}-wide dipole is fed at the center with a sinusoidal wave. The electric current distribution obtained is used to compute the near-field pattern. This distribution is computed on a $(20$-μm$)^2$ box that encloses the dipole. The box is cut with 21 planes in both X and Y directions to match the sampling resolution of our experiment. The electric field is calculated at the cross sections of the intersecting planes. In Fig. 7(a) the result of the simulation is represented in the same scale as that used in Fig. 5(c). By comparing these two figures, we conclude that the deconvolution algorithm can retrieve the location of the two maximum lobes of the dipole antenna. However, the simulated spatial response is less extended and has a more compact distribution. Our simulations show that a finite conductivity of the lossy substrate material tends to broaden the spatial response. The complete explanation of this effect is out of the scope of this paper and will be considered in the future. Keeping the simplified model for the dipole and taking into account the empirical rule pointed out in a previous paper,[6] we have convolved the simulated response with a circular blur having a diameter of one λ_{Si}. The result of the broadening is seen in Fig. 7(b) and can be compared with the antenna spatial response [Fig. 5(c)]. The broadened calculated near-field pattern and the deconvolved spatial response are similar both in shape and in dimension. Both Figs. 5(c) and 7(b) show a charac-

Fig. 7. Dipole antenna modeled in vacuum and having the same relation between length and wavelength as in our case. (a) Calculated near-field distribution. The location of the maximum is the same as in the experimental results. (b) Result of convolving the simulated near-field pattern with a constant function with diameter one λ_{Si}. After this step the distribution can be successfully compared with the experimental results. (c) Result of a simulated 6.7-μm-long, 0.3-μm-wide dipole onto a 1.5-μm-thick layer of SiO_2, $\epsilon = 4.94$, on a semi-infinite substrate of Si, $\epsilon = 11.7$. The scales are the same as those used in Fig. 5.

teristic two-lobe pattern that can be related to the fact that the total length of the dipole antenna is approximately twice the substrate wavelength λ_{Si}. This fact is only visible in the mapping of the spatial response, and it is not obvious from the characteristic parameters shown in Table 1.

A second simulation has been done with a more realistic model. A 6.7-μm-long, 0.3-μm-wide, dipole is located onto a SiO_2 layer having a thickness of 1.5 μm and a dielectric constant of $\epsilon = 4.94$. Under the SiO_2 layer is a semi-infinite Si substrate having a dielectric constant of $\epsilon = 11.7$ (the real thickness of the the silicon substrate is 385 μm). The wavelength of the incident radiation was taken to be $\lambda = 10.6$ μm. The results of this refined model are presented in Fig. 7(c) and can be compared with the experimental results of Fig. 5(c).

From these two simulations, we can conclude that a simple model calculation of the antenna structure, along with an empirical one-wavelength blurring of the result, provides a first-order approach to the pattern of the antenna spatial response. A refined simulation with actual values of material characteristics allows us to obtain a closer approximation to the antenna response. Both approaches can be useful in the evaluation of the design of a given structure.

4. Conclusions

A method for measuring and characterizing the spatial response of a sensor that is nearly a point receiver is presented. It is applied to the measurement of the response of antenna-coupled thin-film MOM diodes for 10.6-μm infrared radiation. This method allows us to obtain a map of the spatial response of an individual device. This map reveals details that are not available by other measurements. For example, it is possible to characterize the spatial response of the coplanar strip lines connecting the detector to the external circuit. Besides, some details regarding the presence of lobes in the near-field antenna pattern are clearly visible. The results can be summarized by parameters describing the aspect ratio, the collection area, or the 50% point of the spatial response, according to the application. Results with this method confirm the previous results for the characterization of MOM detectors. As a practical rule of thumb the collection area of an infrared antenna extends approximately one dielectric wavelength past the physical dimensions of the antenna. The dipole antenna has been simulated and the near-field pattern has been calculated. When this dipole is modeled in vacuum and the obtained results are broadened with a one-wavelength blur function, the simulation and the experimental data agree well both in shape and size. If the antenna is modeled more accurately to the actual case (dipole on a finite-thickness SiO_2 layer and a Si substrate), the results also coincide with the spatial response evaluated from the experimental data by means of the deconvolution method.

References

1. I. Wilke, W. Herrmann, and F. K. Kneubühl, "Integrated nanostrip dipole antennas for coherent 30 THz infrared radiation," Appl. Phys. B **58,** 87–95 (1994).

2. I. Wilke, Y. Oppliger, W. Herrmann, and F. K. Kneubühl, "Nanometer thin-film Ni-NiO-Ni diodes for 30 THz radiation," Appl. Phys. A **58,** 329–341 (1994).

3. C. Fumeaux, W. Herrmann, F. K. Kneubühl, and H. Rothuizen, "Nanometer thin-film Ni-NiO-Ni diodes for detection and mixing of 30 THz radiation," Infrared Phys. Technol. **38,** 123–183 (1998).

4. E. N. Grossman, J. E. Sauvageau, and D. G. McDonald, "Lithographic spiral antennas at short wavelengths," Appl. Phys. Lett. **59,** 3225–3227 (1991).

5. R. J. Hanisch, R. L. White, and R. L. Gilliland, "Deconvolution of Hubble Space Telescope images and spectra," in *Deconvolution of Images and Spectra*, P. A. Janson, ed. (Academic, San Diego, Calif., 1997), pp. 310–360.

6. C. Fumeaux, G. D. Boreman, W. Herrmann, F. K. Kneubühl, and H. Rothuizen, "Spatial impulse response of lithographic infrared antennas," Appl. Opt. **38,** 37–46 (1999).

7. M. B. Schneider and W. W. Webb, "Measurement of submicron laser beam radii," Appl. Opt. **20,** 1382–1388 (1981).

8. J. A. Arnaud, W. M. Hubbard, G. D. Mandeville, B. de la Clavière, E. A. Franke, and J. M. Franke, "Technique for fast measurement of Gaussian laser beam parameters," Appl. Opt. **10,** 2775–2776 (1971).

9. A. E. Siegman, M. W. Sasnett, and T. F. Johnson, "Choice of clip levels for beam width measurements using knife-edge techniques," IEEE J. Quantum Electron. **27,** 1098–1104 (1991).

10. M. Born and E. Wolf, *Principles of Optics*, 6th ed. (Pergamon, Elmsford, NY, 1980), pp. 459–480.

11. V. N. Mahajan, "Uniform versus Gaussian beams: a comparison of the effects of diffraction, obscuration, and aberrations," J. Opt. Soc. Am. A. **3,** 470–485 (1986).

12. J. Alda, J. Alonso, and E. Bernabeu, "Characterization of aberrated laser beams," J. Opt. Soc. Am. A **14,** 2737–2747 (1997).

13. W. H. Richardson, "Bayesian-based iterative method of image restoration," J. Opt. Soc. Am. **62,** 55–59 (1972).

14. L. B. Lucy, "An iterative technique for the rectification of observed distributions," Astron. J. **79,** 745–754 (1974).

15. J. A. Conchello, "Superresolution and convergence properties of the expectation-maximization algorithm for maximum-likelihood deconvolution of incoherent images," J. Opt. Soc. Am. A **15,** 2609–2619 (1998).

16. M. A. Porras, J. Alda, and E. Bernabeu, "Complex beam parameter and *ABCD* law for non-Gaussian and nonspherical light beams," Appl. Opt. **31,** 6389–6402 (1992).

17. C. R. Brewitt-Taylor, D. J. Gunton, and H. D. Rees, "Planar antennas on a dielectric surface," Electron. Lett. **17,** 729–731 (1981).

18. M. N. O. Sadiku, *Numerical Techniques in Electromagnetism*, (CRC Press, Boca Raton, Fla., 1992).